Title

Investigating cerebral perfusion with high resolution hyperpolarized [1-13C]pyruvate MRI

Permalink

https://escholarship.org/uc/item/9tz207d6

Journal

Magnetic Resonance in Medicine, 90(6)

ISSN

0740-3194

Authors

Hu, Jasmine Y
Vaziri, Sana
Bøgh, Nikolaj
et al.

Publication Date

2023-12-01

DOI

10.1002/mrm.29844

Supplemental Material

https://escholarship.org/uc/item/9tz207d6#supplemental

Title:

Investigating Cerebral Perfusion with High Resolution Hyperpolarized [1-^{13}C]Pyruvate MRI

Authors:

Jasmine Y Hu[1,2], Sana Vaziri[1], Nikolaj Bøgh[3], Yaewon Kim[1], Adam W Autry[1], Robert A Bok[1], Yan Li[1,2], Christoffer Laustsen[3], Duan Xu[1,2], Peder EZ Larson[1,2], Susan Chang[4], Daniel B Vigneron[1,2], and Jeremy W Gordon[1]

Affiliations:

[1] Department of Radiology and Biomedical Imaging, University of California San Francisco, San Francisco, California

[2] UC Berkeley-UCSF Graduate Program in Bioengineering, University of California, San Francisco and University of California, Berkeley

[3] MR Research Center, Department of Clinical Medicine, Aarhus University, Aarhus, Denmark

[4] Department of Neurological Surgery, University of California San Francisco, San Francisco, California

Corresponding Author:
Jeremy Gordon
1700 4th St, Byers Hall 102
San Francisco, CA 94158
Email: jeremy.gordon@ucsf.edu
Phone: 415-476-9786

Word Count: 2916

Abstract

Purpose: To investigate high-resolution hyperpolarized (HP) ^{13}C pyruvate MRI for measuring cerebral perfusion in the human brain.

Methods: HP [1-^{13}C]pyruvate MRI was acquired in five healthy volunteers with a multi-resolution EPI sequence with 7.5×7.5 mm^2 resolution for pyruvate. Perfusion parameters were calculated from pyruvate MRI using block-circulant singular value decomposition and compared to relative cerebral blood flow calculated from ASL. To examine regional perfusion patterns, correlations between pyruvate and ASL perfusion were performed for whole brain, gray matter, and white matter voxels.

Results: High resolution 7.5×7.5 mm^2 pyruvate images were used to obtain relative cerebral blood flow (rCBF) values that were significantly positively correlated with ASL rCBF values ($r = 0.48, 0.20, 0.28$ for whole brain, gray matter, and white matter voxels respectively). Whole brain voxels exhibited the highest correlation between pyruvate and ASL perfusion, and there were distinct regional patterns of relatively high ASL and low pyruvate normalized rCBF found across subjects.

Conclusion: Acquiring HP ^{13}C pyruvate metabolic images at higher resolution allows for finer spatial delineation of brain structures and can be used to obtain cerebral perfusion parameters. Pyruvate perfusion parameters were positively correlated to proton ASL perfusion values, indicating a relationship between the two perfusion measures. This HP ^{13}C study demonstrated that hyperpolarized pyruvate MRI can assess cerebral metabolism and perfusion within the same study.

Keywords: Hyperpolarization, MRI, Perfusion, Carbon-13, Pyruvate

Introduction

Hyperpolarized (HP) ^{13}C pyruvate MRI is an emerging tool for non-invasive imaging of metabolism in cancer and disease research, including brain tumors and traumatic brain injury[1–4]. In the brain, HP [1-^{13}C]pyruvate is injected intravenously and rapidly converted to either lactate or bicarbonate, which provides a measure of metabolic preference for either glycolysis or oxidative phosphorylation, respectively. Both lactate and bicarbonate are produced in normal brain metabolism, and an increase in lactate and decrease in bicarbonate has been observed in brain tumor lesions[1,2]. By measuring changes in metabolism, HP pyruvate is an emerging imaging probe for measuring metabolic reprogramming in brain tumors.

Perfusion is also an important metric for brain tumors, used for tumor grading, tracking treatment response, and distinguishing pseudoprogression from recurrent tumor[5–7]. MR perfusion imaging types include dynamic susceptibility contrast (DSC), dynamic contrast-enhanced (DCE), and arterial spin labeling (ASL)[8]. DSC and DCE involve intravenous gadolinium contrast to measure cerebral blood flow (CBF) and capillary permeability respectively, while ASL labels inflowing blood to measure CBF. HP pyruvate imaging is similar to these imaging techniques, involving rapid imaging of a contrast agent that perfuses into tissue and is metabolized. HP pyruvate has been investigated preclinically for measuring perfusion in brain tumor xenografts[9], the myocardium[10], ischemic stroke[11,12], and acute kidney injury[13,14]. Recent improvement to in-plane spatial resolution (from 15 × 15 to 7.5 × 7.5 mm^2) for clinical HP pyruvate research studies has enabled better localization and quantitation of metabolic rate constants by acquiring the injected pyruvate at a four-fold finer spatial resolution than its lower SNR metabolic products lactate and bicarbonate[15,16]. A prior study measuring pyruvate-to-lactate conversion rates (k_{PL}) at coarse and fine spatial resolutions demonstrated a mean difference in k_{PL} of more than 75% for voxels near arteries and veins due to the ability to better separate pyruvate vascular signals from intracellular pyruvate in brain parenchyma with the finer spatial resolution[15]. The improved ability to depict the vasculature at the higher spatial resolution indicated that this approach might also be used to provide regional perfusion metrics within the same imaging dataset. The purpose of this study was to investigate high-resolution HP ^{13}C pyruvate MRI for measuring cerebral perfusion in the human brain with the motivation that assessing both metabolism and perfusion within a single hyperpolarized MRI could ultimately be valuable for monitoring changes in disease progression and response. To assess cerebral perfusion with hyperpolarized pyruvate, high-resolution [1-^{13}C]pyruvate studies were acquired in healthy human brains and the resulting pyruvate perfusion parameters were compared to ^{1}H ASL perfusion values.

Methods

A total of six HP brain studies were performed in four healthy human volunteer subjects following informed consent according to University of California San Francisco IRB and FDA IND approved protocols (IRB 17-21951, IND 137553). The mean age of the subjects was 41 years (range 37-47 years) and all subjects were male. [1-^{13}C]Pyruvate solutions were prepared as described previously[15] according to good manufacturing practice and injected after release by a pharmacist (0.43 mL/kg dose of 250 mM pyruvate at 5 mL/s, 20 mL sterile saline flush). Studies were performed on a 3T MR scanner (MR750, GE Healthcare) using an integrated 8-channel ^{1}H/ 24-channel ^{13}C phased array receiver with an 8-rung low-pass ^{13}C volume transmit coil (Rapid Biomedical, Würzburg, Germany). Hyperpolarized ^{13}C data were acquired with a metabolite-selective imaging approach, using a singleband spectral-spatial RF pulse for excitation (passband FWHM = 130 Hz, stopband = 868 Hz) and a single-shot symmetric echoplanar readout for encoding[17] (TR = 125 ms, TE = 30.7 ms, 32 × 32 matrix size, BW = ±19.23 kHz, 1.064 ms echo-spacing, and 8 slices with an axial orientation). Pyruvate was excited with a 20° flip angle and lactate and bicarbonate were excited with a 30° flip angle. The lower flip angle for pyruvate and higher flip angles for lactate and bicarbonate were used to reduce the saturation of pyruvate and compensate for the lower SNR of downstream metabolites lactate and bicarbonate. The in-plane spatial resolution for each metabolite was changed by independently scaling the encoding gradients, resulting in 7.5×7.5 mm^2 resolution for pyruvate and 15×15 mm^2 resolution for lactate and bicarbonate; the slice thickness was maintained at 15 mm. Pyruvate was acquired at a higher resolution than its downstream metabolites to mitigate the tradeoff between finer spatial resolution and detectability of low SNR metabolites. For one subject, a second HP [1-^{13}C]pyruvate study was acquired with 15×15 mm^2 resolution for all metabolites. This constant resolution study was only used for intra-subject comparison and was not included in correlations of high-resolution studies. Twenty time points were acquired with a 3 s temporal resolution for a total scan time of one minute. Data acquisition started 5 s after the end of the saline injection for the first two subjects and immediately after the end of the saline injection for the latter two subjects. Immediately following imaging, a non-localized spectrum was acquired to confirm the center frequency was set correctly. For proton perfusion, 3D pulsed continuous ASL was acquired (TR = 4846 ms, TE = 10.5 ms, FOV = 256 mm, BW = 125 kHz, 2025 ms post-label delay, and 128 × 128 × 72 matrix size, 2 × 2 × 4 mm^3 resolution). For anatomic reference, ^1H 3D inversion-recovery spoiled gradient-recalled echo (IR-SPGR; TR = 6.7 ms, TE = 2.5 ms, TI = 450 ms, 25.6 × 25.6 × 18.6 cm^2 FOV, 256 × 256 × 124 matrix size, 1 × 1 × 1.5 mm^3 resolution) images were acquired with the dual-tuned coil.

The ^{13}C EPI data were reconstructed using the Orchestra toolbox (GE Healthcare). Multichannel data were pre-whitened[18] and then coil combined using pyruvate to estimate the coil weights[19]. Denoising was performed on the coil-combined data using global-local higher-order singular value decomposition (GL-HOSVD) as described by Kim et al. for HP ^{13}C MRI[20]. Lactate and bicarbonate images were cropped and zero padded to match the pyruvate FOV and matrix size, and signal values were normalized by voxel volume to account for the different acquisition resolutions. To obtain relative cerebral blood flow (rCBF) maps, ASL perfusion-weighted images were divided by proton density images[21]. ASL rCBF maps were resampled to the pyruvate voxel size using tri-linear interpolation. Gray and white matter masks were segmented on T_1-weighted images, with the cortex being excluded from the white matter masks using the Automated Anatomical Atlas 3[22]. Voxels containing at least 90% brain, 50% gray matter, or 50% white matter were included in Pearson correlation analysis. Proton images were used in the FSL FAST algorithm[23] to generate brain masks, and the proton images were also summed in the slice dimension to match the carbon slice thickness.

To remove coil shading, bias correction using N4ITK[24] was performed on HP ^{13}C images. To obtain ^{13}C bias fields, lactate area-under-curve (AUC) images were brain-masked and supplied as input for the N4ITK algorithm using 3 layers of 100 iterations, convergence threshold of 0 to run all iterations, *B*-spline order of 3, and a shrink factor of 1. The resulting bias fields were then used to correct HP ^{13}C images before perfusion calculation. Pyruvate AUC images were not used as input for the bias correction algorithm because doing so resulted in bias maps weighted on large blood vessels and not the intended coil shading as shown in Figure S1. ASL rCBF maps did not require bias-correction because of the division of proton density images from the same coil. To visually compare pyruvate and ASL rCBF maps at similar resolutions, pyruvate rCBF maps for one subject were zerofilled twice to match ASL in-plane resolution and Fermi filtered to remove ringing artifacts.

HP pyruvate perfusion parameters were obtained by analyzing the dynamic pyruvate images with the Dynamic Susceptibility Contrast MRI toolbox (https://github.com/marcocastellaro/dsc-mri-toolbox). As many as four voxels were automatically selected to fit an arterial input function[25]. Relative cerebral blood volume (rCBV) was calculated by taking the integral of the dynamic pyruvate signal normalized by the arterial input function. rCBF and mean transit time (MTT) were calculated using block-circulant singular value decomposition and MTT was corrected for depolarization using a single $T_1 = 30$ s[26]. Total carbon perfusion parameters were also calculated using dynamic pyruvate, lactate, and bicarbonate images corrected for respective flip angles and summed over metabolites. Voxels with pyruvate or total carbon rCBF greater than 0.25 arbitrary units (a.u.) were excluded from correlation because the voxel locations were within the superior sagittal sinus or cerebral arteries. Min-max normalization was used to compare pyruvate and ASL rCBF values on the same scale. Kinetic rate constants for each voxel were computed using an inputless two-site model to generate quantitative maps of pyruvate-to-lactate conversion (k_{PL}) from images that were not bias-corrected[15,27]. Pyruvate area-under-curve (AUC) maps were also generated and bias-corrected with the same bias fields used for dynamic HP ^{13}C images. Voxel values including ASL rCBF, pyruvate rCBF, pyruvate rCBV, pyruvate AUC, and k_{PL} were compared using Pearson correlation and paired two-tailed t-tests. Average correlation coefficients were calculated using the Fisher transformation.

Results

The dynamic time-course of high-resolution 7.5 × 7.5 mm^2 pyruvate images in Figure 1 shows the arrival and perfusion of the pyruvate bolus into the cerebral vessels and brain tissue. The arterial pyruvate signal quickly decreased within the first 15 s after the bolus arrival, while the venous signal in the superior sagittal sinus continued through the 60 s acquisition. Pyruvate signal was higher in gray matter than in white matter.

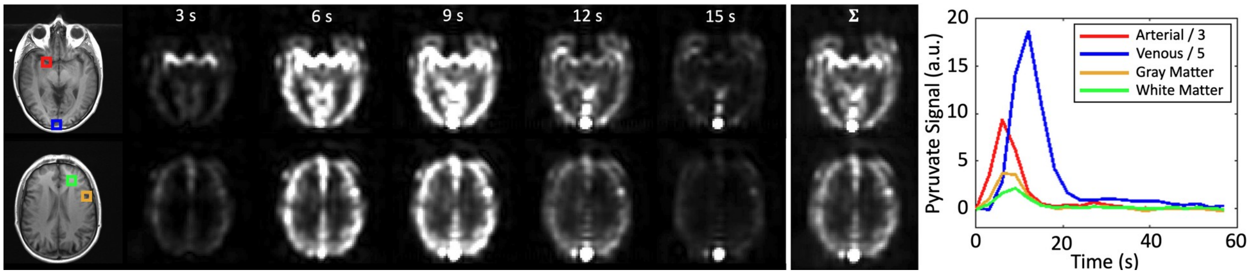

Figure 1. Dynamic [1-^{13}C]pyruvate perfusion. Dynamic 7.5 × 7.5 mm^2 [1-^{13}C]pyruvate images, area-under-curve images (Σ), and time-course plot of arterial, venous, white matter and gray matter voxels in a representative subject. Pyruvate signal in the middle cerebral arteries quickly decreased within the first 15 s of the bolus arrival, while the venous signal in the superior sagittal sinus continued through the acquisition. Pyruvate images were bias-corrected and zerofilled once for display. Intensity units are arbitrary.

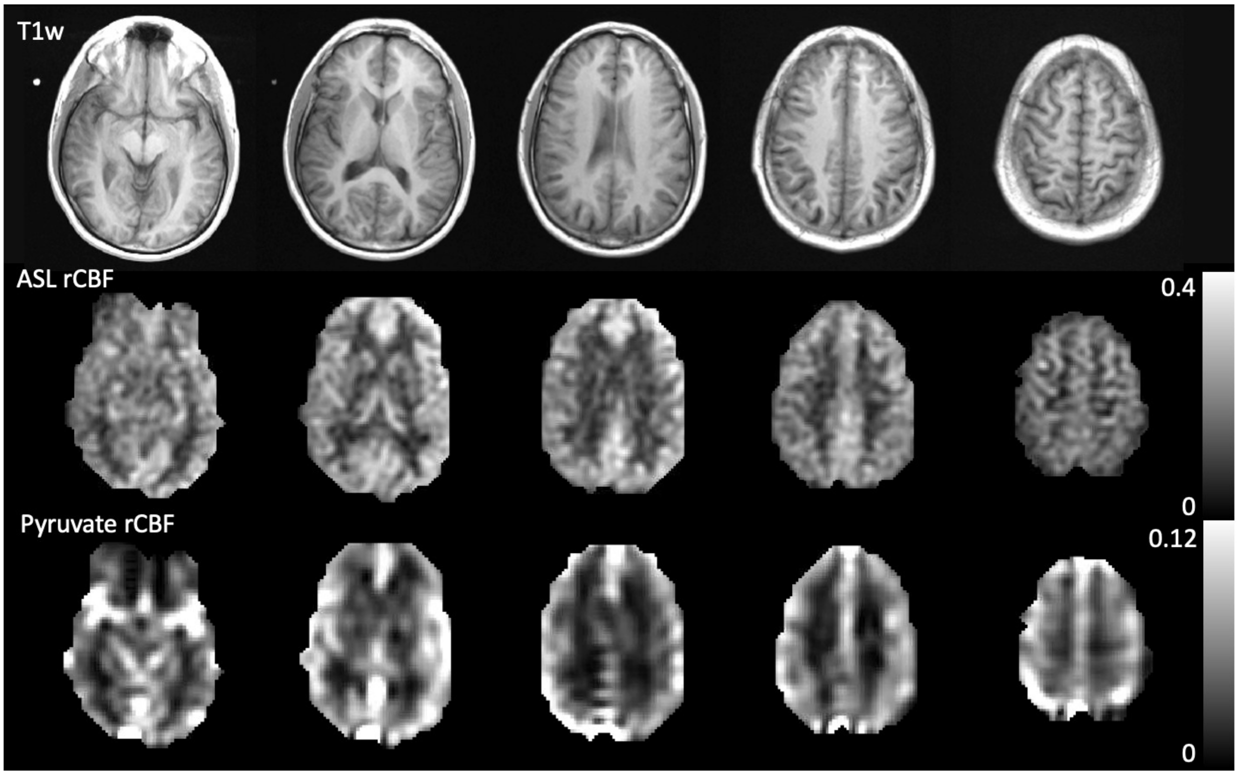

Figure 2. ASL versus [1-^{13}C]pyruvate rCBF. Maps of relative cerebral blood flow (rCBF) from ASL and [1-^{13}C]pyruvate with reference proton images from a representative subject. Both rCBF maps exhibit higher flow in the gray matter than in the white matter. Pyruvate rCBF maps have large signals from the middle cerebral arteries and superior sagittal sinus. ASL maps were

summed in the slice direction to match the pyruvate slice thickness and brain-masked. Pyruvate maps were zerofilled twice to match ASL in-plane resolution, Fermi filtered to remove ringing artifacts, and brain-masked for display. All units are arbitrary.

High-resolution pyruvate images were used to calculate rCBF maps, shown in Figure 2 along with ASL rCBF maps. Both rCBF maps were characterized by higher flow in the gray matter than in the white matter. Pyruvate rCBF maps demonstrated large signals from the middle cerebral arteries and the anterior and posterior portions of the superior sagittal sinus. This blood vessel weighting is even more pronounced in pyruvate rCBF maps obtained from coarse-resolution (15 × 15 mm^2) images, as shown in Figure S2, where the greatest differences are located near the arteries, veins, and gray matter. Total carbon rCBF was also calculated from summed pyruvate, lactate, and bicarbonate images, with the resulting rCBF values shown in Figure S3 being approximately the same as rCBF values calculated from pyruvate alone.

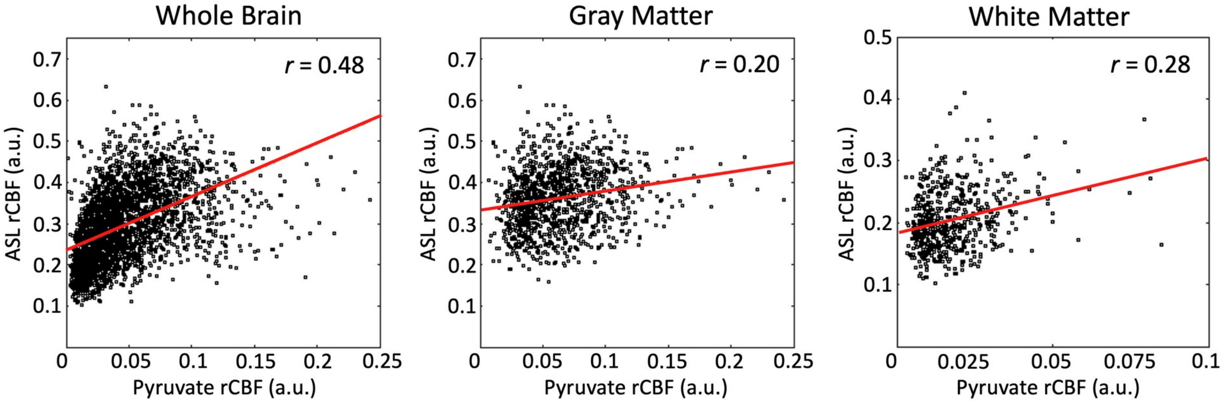

Figure 3. **Regional ASL and [1-^{13}C]pyruvate rCBF correlations.** rCBF versus ASL rCBF linear correlation coefficients and scatterplots for voxels from all subjects (*n* = 4) acquired at high resolution (*n* = 5), by respective mask (3024 whole brain, 1169 gray matter, and 575 white matter voxels all from 2 central slices of the brain). Voxels with pyruvate rCBF > 0.25 a.u. were excluded due to their being within the superior sagittal sinus and cerebral arteries. Linear regression fits are plotted in red. Whole brain voxels exhibited the highest correlation between pyruvate and ASL rCBF, and gray matter voxel correlations exhibited more spread than white matter voxel correlations. Voxels with high ASL rCBF and moderate pyruvate rCBF (upper left of whole brain and gray matter plots) were located in the precuneus region. Voxels with moderate ASL rCBF and high pyruvate rCBF (far right of whole brain and gray matter plots) were located near cerebral blood vessels. All correlation coefficients were significant ($p <$ 0.0001) and all units are arbitrary.

To compare perfusion between ASL and pyruvate-derived metrics on a regional basis, we generated linear correlation coefficients and scatterplots shown in Figure 3. Figure 3 summarizes correlations from all subjects (*n* = 4) and all high-resolution studies (*n* = 5), by respective mask (3024 whole-brain, 1169 gray matter, and 575 white matter voxels, all from 2 central slices of the brain). Whole brain voxels exhibited the greatest correlation between pyruvate and ASL rCBF, and gray matter voxels were also moderately correlated with more spread than white matter. Voxels with high ASL rCBF and low pyruvate rCBF were located in the precuneus region. Voxels with moderate ASL rCBF and high pyruvate rCBF were located near cerebral blood vessels. Correlation coefficients were consistent across individual studies and brain masks, as summarized in Table 1. High resolution pyruvate rCBF exhibited higher correlations to ASL rCBF than coarse resolution pyruvate rCBF for all brain masks as shown in Figure S4 for two resolutions of pyruvate data collected from the same subject.

To explore the high correlations within whole brain further, Figure 4 shows correlation plots and coefficients for ASL versus pyruvate perfusion and metabolic parameters from whole brain voxels from a representative study. Pyruvate rCBF, pyruvate rCBV, and pyruvate AUC were significantly correlated to ASL rCBF and to each other. These trends were also reflected for gray matter and white matter as shown in Tables S1-S3. Pyruvate-to-lactate conversion (k_{PL}) was not correlated to ASL rCBF but was negatively correlated to pyruvate rCBF, rCBV, and AUC.

To directly examine the differences between ASL and pyruvate rCBF on a voxel-wise basis, we calculated the percent difference of normalized ASL and pyruvate rCBF shown in Figure 5. Normalized ASL and pyruvate rCBF measurements are more closely matched in white matter than in gray matter. Overall normalized ASL rCBF is higher than normalized pyruvate rCBF, particularly in the precuneus region.

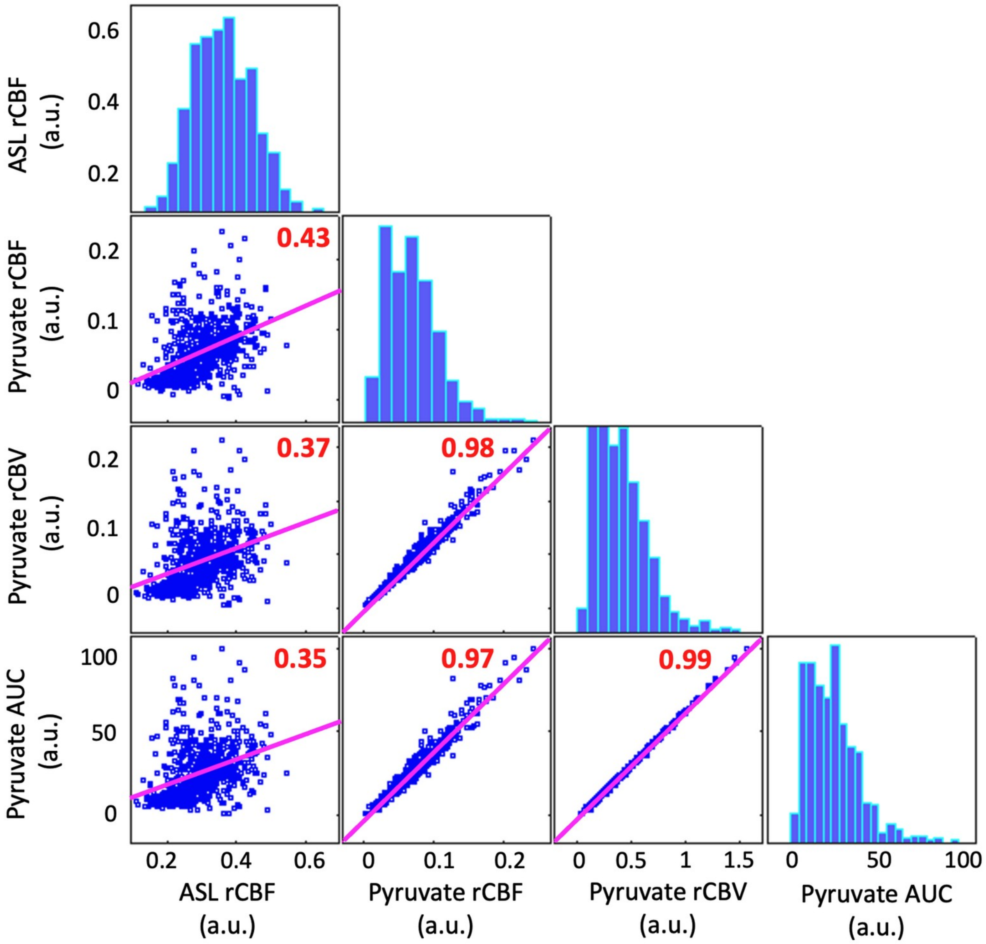

Figure 4. Multi-parametric ASL and [1-^{13}C]pyruvate correlations. Correlation plots and coefficients for ASL versus pyruvate perfusion and metabolic parameters from whole brain voxels from a representative study. All coefficient values were significant ($p < 0.05$). Linear regression fits are plotted in magenta. Pyruvate rCBF, rCBV, and area-under-curve (AUC) were highly correlated to ASL rCBF. Pyruvate AUC was highly correlated with pyruvate rCBV, which affirms AUC as a model-free perfusion metric. Pyruvate rCBF and pyruvate rCBV are strongly correlated to each other, which is due to their calculation from the same input data.

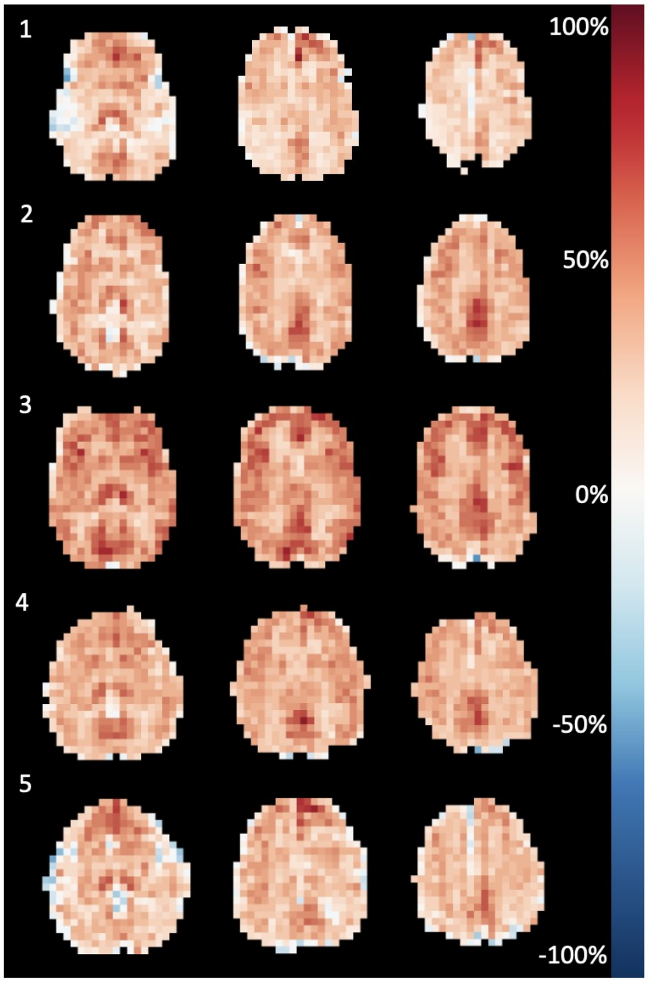

Figure 5. **Percent Difference of ASL and [1-^{13}C]pyruvate rCBF**. Percent difference map of ASL and pyruvate normalized rCBF for all high-resolution studies. Studies 4 and 5 were acquired two years apart from the same subject. Normalized ASL and pyruvate rCBF measurements were more closely matched in white matter than in gray matter. The precuneus region demonstrated consistently elevated normalized ASL rCBF as compared to pyruvate rCBF.

Discussion

In this study, we utilized high resolution pyruvate images to obtain cerebral perfusion and metabolism parameters. The highest pyruvate signal and flow was in blood vessels, which was reflected in pyruvate rCBF maps by high weighting near the middle cerebral arteries and the anterior and posterior portions of the superior sagittal sinus. Pyruvate rCBF maps exhibited higher flow in gray matter than in white matter, similar to what was observed in ASL rCBF maps. High resolution pyruvate rCBF exhibited higher correlation to ASL rCBF than coarse resolution pyruvate rCBF, indicating that high resolution pyruvate improves the precision of perfusion calculation by reducing partial volume effects. These findings are supported by previous results in Hu et al.[15] comparing kinetic conversion rates calculated from high and coarse resolution pyruvate MRI. When examining regional differences between ASL and pyruvate rCBF, normalized white matter rCBF was closer to normalized ASL rCBF than gray matter rCBF. This pattern was continued in the linear correlations between ASL and pyruvate rCBF, where white matter rCBF values exhibited higher correlations than gray matter rCBF for the majority of individual studies and for all studies combined. This correlation difference between gray and white matter may be due to the distribution and thickness of each brain matter type in relation to the voxel size of HP pyruvate images. The 7.5×7.5 mm^2 resolution was greater than the thickness of cortical gray matter, which has been reported in the literature to average 2.5 mm (range 1-4.5 mm)[28]. Gray matter voxels can also include cerebral blood vessels with much higher signals, though we have attempted to exclude those voxels using a pyruvate rCBF threshold. The white matter region is large in comparison to gray matter, which makes it a consistent region to record measurements. In addition to partial volume effects, increased pyruvate metabolism in gray matter as compared to white matter could contribute to the extent of pyruvate and ASL rCBF correlation for each region[29,30]. HP lactate and bicarbonate signals in the precuneus were among the highest in a topography study of normal human brains[30], suggesting that elevated metabolism in the precuneus[31,32] could affect the HP pyruvate signal. We further explored regional perfusion relationships by correlating ASL rCBF and additional pyruvate perfusion parameters. Pyruvate AUC was strongly correlated to both ASL and pyruvate perfusion metrics which affirms pyruvate AUC as a model-free perfusion metric.

HP pyruvate can be used to obtain both cerebral perfusion and metabolism measurements, but this study had some limitations. In addition to perfusion, the HP pyruvate signal is affected by magnetization utilization, T_1 decay, and metabolism during the acquisition time frame. The use of the arterial input function to calculate perfusion metrics normalizes for magnetization utilization and T_1 decay, and we assumed that the impact of metabolism on the bulk pyruvate signal is negligible. To verify the impact of metabolism, we have used the total carbon-13 signal from all HP metabolites to also calculate perfusion and found that the resulting measurements were almost identical to those calculated from only pyruvate signals. To remove coil shading in

HP images, lactate AUC images were used in N4ITK bias correction to generate bias field maps. Pyruvate AUC images were not used because doing so resulted in bias fields heavily weighted by large pyruvate signals in the anterior and posterior portions of the superior sagittal sinus as shown in Figure S1. The number of datasets in this study was limited and we plan to acquire datasets in a larger cohort to refine our results and provide further evidence establishing the value of high resolution HP pyruvate MRI.

This work is the first to use high resolution HP pyruvate images to estimate perfusion in human brains. Preclinical studies have used HP pyruvate to measure cerebral perfusion[9,10], as well as co-polarizations of pyruvate and urea for simultaneous metabolism and perfusion measurements[33,34]. ^{13}C-labeled urea is a perfusion agent that is currently under investigation in human studies and may offer a promising means of improving the HP perfusion measurements shown here[35]. Because urea functions as a metabolically inactive and extracellular perfusion agent, its signal represents blood flow and perfusion without the effects of metabolic conversion[36,37]. With the combination of high-resolution imaging[16], denoising[20], and bias correction[24], HP pyruvate provides spatially detailed and unique perfusion measurements that have further opportunities for enhancement with co-polarized urea.

While there was high correlation between the overall ASL and [1-^{13}C]pyruvate rCBF, regional variations in the rCBF measured with the two approaches may provide insight into regions of elevated or altered metabolism that could augment the standard radiometric and kinetic modeling analyses. Indeed, a recent study by Grist et al. introduced a metabolic clearance rate and fractional metabolism analysis framework for HP ^{13}C MRI, which combines the CBF values from gadolinium and pyruvate imaging to determine the relative contribution of metabolism to the pyruvate signal[12]. This approach would be applicable to the ASL and pyruvate data acquired here and could also be readily performed using co-polarized pyruvate and urea imaging[35], reducing the need for a separate Gd injection and/or a separate perfusion-weighted scan.

Conclusions

Acquiring HP ^{13}C pyruvate metabolic images at high resolution allows for finer spatial delineation of brain structures and can be used to obtain cerebral perfusion parameters. Pyruvate perfusion parameters were positively correlated to proton ASL perfusion values, indicating a relationship between the two perfusion measures. This HP ^{13}C study showed that hyperpolarized pyruvate MRI can be used to assess cerebral metabolism and perfusion within the same study.

Acknowledgements

This research was supported by NIH grants (PO1CA118816, U01EB026412, P41EB013598), the UCSF NICO project, and the Lundbeck Foundation. We thank Luis A. Torres, Sean B. Fain, and Andrew D. Hahn for helpful discussions regarding bias correction using N4ITK.

References

1. Autry AW, Gordon JW, Chen HY, et al. Characterization of serial hyperpolarized 13C metabolic imaging in patients with glioma. *NeuroImage: Clinical*. 2020;27:102323. doi:10.1016/j.nicl.2020.102323

2. Park I, Larson PEZ, Gordon JW, et al. Development of methods and feasibility of using hyperpolarized carbon-13 imaging data for evaluating brain metabolism in patient studies: Hyperpolarized Carbon-13 Metabolic Imaging of Patients With Brain Tumors. *Magn Reson Med*. 2018;80(3):864-873. doi:10.1002/mrm.27077

3. Miloushev VZ, Granlund KL, Boltyanskiy R, et al. Metabolic Imaging of the Human Brain with Hyperpolarized ^{13} C Pyruvate Demonstrates ^{13} C Lactate Production in Brain Tumor Patients. *Cancer Res*. 2018;78(14):3755-3760. doi:10.1158/0008-5472.CAN-18-0221

4. Hackett EP, Pinho MC, Harrison CE, et al. Imaging Acute Metabolic Changes in Patients with Mild Traumatic Brain Injury Using Hyperpolarized [1-13C]Pyruvate. *iScience*. 2020;23(12):101885. doi:10.1016/j.isci.2020.101885

5. Wen PY, Weller M, Lee EQ, et al. Glioblastoma in adults: a Society for Neuro-Oncology (SNO) and European Society of Neuro-Oncology (EANO) consensus review on current management and future directions. *Neuro Oncol*. 2020;22(8):1073-1113. doi:10.1093/neuonc/noaa106

6. Ellingson BM, Bendszus M, Boxerman J, et al. Consensus recommendations for a standardized Brain Tumor Imaging Protocol in clinical trials. *Neuro Oncol*. 2015;17(9):1188-1198. doi:10.1093/neuonc/nov095

7. Thust SC, van den Bent MJ, Smits M. Pseudoprogression of brain tumors. *J Magn Reson Imaging*. 2018;48(3):571-589. doi:10.1002/jmri.26171

8. Villanueva-Meyer JE, Mabray MC, Cha S. Current Clinical Brain Tumor Imaging. *Neurosurgery*. 2017;81(3):397-415. doi:10.1093/neuros/nyx103

9. Park I, Lupo JM, Nelson SJ. Correlation of Tumor Perfusion Between Carbon-13 Imaging with Hyperpolarized Pyruvate and Dynamic Susceptibility Contrast MRI in Pre-Clinical Model of Glioblastoma. *Mol Imaging Biol*. 2019;21(4):626-632. doi:10.1007/s11307-018-1275-y

10. Fuetterer M, Busch J, Traechtler J, et al. Quantitative myocardial first-pass cardiovascular magnetic resonance perfusion imaging using hyperpolarized [1-13C] pyruvate. *J Cardiovasc Magn Reson*. 2018;20(1):73. doi:10.1186/s12968-018-0495-2

11. Bøgh N, Olin RB, Hansen ES, et al. Metabolic MRI with hyperpolarized [1-13C]pyruvate separates benign oligemia from infarcting penumbra in porcine stroke. *J Cereb Blood Flow Metab*. 2021;41(11):2916-2927. doi:10.1177/0271678X211018317

12. Grist JT, Bøgh N, Hansen ES, et al. Developing a metabolic clearance rate framework as a translational analysis approach for hyperpolarized 13C magnetic resonance imaging. *Sci Rep*. 2023;13(1):1613. doi:10.1038/s41598-023-28643-8

13. Lindhardt JL, Nielsen PM, Hansen ESS, et al. The hemodynamic and metabolic effects of spironolactone treatment in acute kidney injury assessed by hyperpolarized MRI. *NMR Biomed*. 2020;33(10):e4371. doi:10.1002/nbm.4371

14. Mariager CØ, Lindhardt J, Nielsen PM, Schulte RF, Ringgaard S, Laustsen C. Fractional Perfusion: A Simple Semi-Parametric Measure for Hyperpolarized 13C MR. *IEEE Transactions on Radiation and Plasma Medical Sciences*. 2019;3(4):523-527. doi:10.1109/TRPMS.2019.2905724

15. Hu JY, Kim Y, Autry AW, et al. Kinetic analysis of multi-resolution hyperpolarized 13 C human brain MRI to study cerebral metabolism. *Magn Reson Med*. 2022;88(5):2190-2197. doi:10.1002/mrm.29354

16. Gordon JW, Autry AW, Tang S, et al. A variable resolution approach for improved acquisition of hyperpolarized ^{13} C metabolic MRI. *Magn Reson Med*. 2020;84(6):2943-2952. doi:10.1002/mrm.28421

17. Gordon JW, Chen HY, Autry A, et al. Translation of Carbon-13 EPI for hyperpolarized MR molecular imaging of prostate and brain cancer patients. *Magn Reson Med*. 2019;81(4):2702-2709. doi:10.1002/mrm.27549

18. Pruessmann KP, Weiger M, Börnert P, Boesiger P. Advances in sensitivity encoding with arbitrary k-space trajectories. *Magn Reson Med*. 2001;46(4):638-651. doi:10.1002/mrm.1241

19. Zhu Z, Zhu X, Ohliger MA, et al. Coil combination methods for multi-channel hyperpolarized 13C imaging data from human studies. *Journal of Magnetic Resonance*. 2019;301:73-79. doi:10.1016/j.jmr.2019.01.015

20. Kim Y, Chen HY, Autry AW, et al. Denoising of hyperpolarized 13 C MR images of the human brain using patch-based higher-order singular value decomposition. *Magn Reson Med*. Published online June 25, 2021. doi:10.1002/mrm.28887

21. Buxton RB, Frank LR, Wong EC, Siewert B, Warach S, Edelman RR. A general kinetic model for quantitative perfusion imaging with arterial spin labeling. *Magnetic Resonance in Medicine*. 1998;40(3):383-396. doi:10.1002/mrm.1910400308

22. Rolls ET, Huang CC, Lin CP, Feng J, Joliot M. Automated anatomical labelling atlas 3. *NeuroImage*. 2020;206:116189. doi:10.1016/j.neuroimage.2019.116189

23. Zhang Y, Brady M, Smith S. Segmentation of brain MR images through a hidden Markov random field model and the expectation-maximization algorithm. *IEEE Trans Med Imaging*. 2001;20(1):45-57. doi:10.1109/42.906424

24. Tustison NJ, Avants BB, Cook PA, et al. N4ITK: improved N3 bias correction. *IEEE Trans Med Imaging*. 2010;29(6):1310-1320. doi:10.1109/TMI.2010.2046908

25. Peruzzo D, Bertoldo A, Zanderigo F, Cobelli C. Automatic selection of arterial input function on dynamic contrast-enhanced MR images. *Computer Methods and Programs in Biomedicine*. 2011;104(3):e148-e157. doi:10.1016/j.cmpb.2011.02.012

26. Johansson E, Månsson S, Wirestam R, et al. Cerebral perfusion assessment by bolus tracking using hyperpolarized 13C. *Magnetic Resonance in Medicine*. 2004;51(3):464-472. doi:10.1002/mrm.20013

27. Mammoli D, Gordon J, Autry A, et al. Kinetic Modeling of Hyperpolarized Carbon-13 Pyruvate Metabolism in the Human Brain. *IEEE Trans Med Imaging*. 2020;39(2):320-327. doi:10.1109/TMI.2019.2926437

28. Fischl B, Dale AM. Measuring the thickness of the human cerebral cortex from magnetic resonance images. *Proceedings of the National Academy of Sciences*. 2000;97(20):11050-11055. doi:10.1073/pnas.200033797

29. Grist JT, McLean MA, Riemer F, et al. Quantifying normal human brain metabolism using hyperpolarized [1–13C]pyruvate and magnetic resonance imaging. *NeuroImage*. 2019;189:171-179. doi:10.1016/j.neuroimage.2019.01.027

30. Lee CY, Soliman H, Geraghty BJ, et al. Lactate topography of the human brain using hyperpolarized 13C-MRI. *NeuroImage*. 2020;204:116202. doi:10.1016/j.neuroimage.2019.116202

31. Goyal MS, Vlassenko AG, Blazey TM, et al. Loss of Brain Aerobic Glycolysis in Normal Human Aging. *Cell Metab*. 2017;26(2):353-360.e3. doi:10.1016/j.cmet.2017.07.010

32. Vaishnavi SN, Vlassenko AG, Rundle MM, Snyder AZ, Mintun MA, Raichle ME. Regional aerobic glycolysis in the human brain. *Proc Natl Acad Sci U S A*. 2010;107(41):17757-17762. doi:10.1073/pnas.1010459107

33. Qin H, Tang S, Riselli AM, et al. Clinical translation of hyperpolarized ^{13} C pyruvate and urea MRI for simultaneous metabolic and perfusion imaging. *Magnetic Resonance in Med*. 2022;87(1):138-149. doi:10.1002/mrm.28965

34. Lau AZ, Miller JJ, Robson MD, Tyler DJ. Simultaneous assessment of cardiac metabolism and perfusion using copolarized [1- ^{13} C]pyruvate and ^{13} C-urea. *Magn Reson Med*. 2017;77(1):151-158. doi:10.1002/mrm.26106

35. Liu X, Tang S, Mu C, et al. Development of specialized magnetic resonance acquisition techniques for human hyperpolarized [13 C,15 N2]urea + [1-13 C]pyruvate simultaneous perfusion and metabolic imaging. *Magn Reson Med*. 2022;88(3):1039-1054. doi:10.1002/mrm.29266

36. von Morze C, Larson PEZ, Hu S, et al. Investigating tumor perfusion and metabolism using multiple hyperpolarized (13)C compounds: HP001, pyruvate and urea. *Magn Reson Imaging*. 2012;30(3):305-311. doi:10.1016/j.mri.2011.09.026

37. von Morze C, Larson PEZ, Hu S, et al. Imaging of Blood Flow Using Hyperpolarized [13C]Urea in Preclinical Cancer Models. *J Magn Reson Imaging*. 2011;33(3):692-697. doi:10.1002/jmri.22484

Table

Table 1. Regional rCBF correlation coefficients for pyruvate rCBF and ASL rCBF.

Study	**Whole brain**	**Gray matter**	**White matter**
1	0.61	0.36	0.37
2	0.63	0.24	0.32
3	0.38	0.38	0.26
4	0.41	0.12	0.46
5	0.44	0.17	0.34
Average	**0.50 ± 0.12**	**0.26 ± 0.11**	**0.35 ± 0.07**

Note: All Pearson correlation coefficients were significant ($p < 10^{-5}$). Studies 4 and 5 were acquired two years apart from the same subject. Averages were calculated using Fisher transformation.

Figure Legends

Figure 1. Dynamic [1-^{13}C]pyruvate perfusion. Dynamic 7.5 × 7.5 mm^2 [1-^{13}C]pyruvate images, area-under-curve images (Σ), and time-course plot of arterial, venous, white matter and gray matter voxels in a representative subject. Pyruvate signal in the middle cerebral arteries quickly decreased within the first 15 s of the bolus arrival, while the venous signal in the superior sagittal sinus continued through the acquisition. Pyruvate images were bias-corrected and zerofilled once for display. Intensity units are arbitrary.

Figure 2. ASL versus [1-^{13}C]pyruvate rCBF. Maps of relative cerebral blood flow (rCBF) from ASL and [1-^{13}C]pyruvate with reference proton images from a representative subject. Both rCBF maps exhibit higher flow in the gray matter than in the white matter. Pyruvate rCBF maps have large signals from the middle cerebral arteries and superior sagittal sinus. ASL maps were summed in the slice direction to match the pyruvate slice thickness and brain-masked. Pyruvate maps were zerofilled twice to match ASL in-plane resolution, Fermi filtered to remove ringing artifacts, and brain-masked for display. All units are arbitrary.

Figure 3. Regional ASL and [1-^{13}C]pyruvate rCBF correlations. rCBF versus ASL rCBF linear correlation coefficients and scatterplots for voxels from all subjects ($n = 4$) acquired at high resolution ($n = 5$), by respective mask (3024 whole brain, 1169 gray matter, and 575 white matter voxels all from 2 central slices of the brain). Voxels with pyruvate rCBF > 0.25 a.u. were excluded due to their being within the superior sagittal sinus and cerebral arteries. Linear regression fits are plotted in red. Whole brain voxels exhibited the highest correlation between pyruvate and ASL rCBF, and gray matter voxel correlations exhibited more spread than white matter voxel correlations. Voxels with high ASL rCBF and moderate pyruvate rCBF (upper left of whole brain and gray matter plots) were located in the precuneus region. Voxels with moderate ASL rCBF and high pyruvate rCBF (far right of whole brain and gray matter plots) were located near cerebral blood vessels. All correlation coefficients were significant ($p < 0.0001$) and all units are arbitrary.

Figure 4. Multi-parametric ASL and [1-^{13}C]pyruvate correlations. Correlation plots and coefficients for ASL versus pyruvate perfusion and metabolic parameters from whole brain voxels from a representative study. All coefficient values were significant ($p < 0.05$). Linear regression fits are plotted in magenta. Pyruvate rCBF, rCBV, and area-under-curve (AUC) were highly correlated to ASL rCBF. Pyruvate AUC was highly correlated with pyruvate rCBV,

which affirms AUC as a model-free perfusion metric. Pyruvate rCBF and pyruvate rCBV are strongly correlated to each other, which is due to their calculation from the same input data.

Figure 5. Percent Difference of ASL and [1-^{13}C]pyruvate rCBF. Percent difference map of ASL and pyruvate normalized rCBF for all high-resolution studies. Studies 4 and 5 were acquired two years apart from the same subject. Normalized ASL and pyruvate rCBF measurements were more closely matched in white matter than in gray matter. The precuneus region demonstrated consistently elevated normalized ASL rCBF as compared to pyruvate rCBF.

Supporting Information Legends

Figure S1. Comparison of bias fields generated from pyruvate area-under-curve (AUC) versus lactate AUC. The pyruvate bias field is weighted primarily in the anterior and posterior portions of the superior sagittal sinus. The lactate bias field is qualitatively similar to the expected coil profile with weighting around the edges of the brain. Intensity values have arbitrary units.

Figure S2. Coarse versus high resolution [1-^{13}C]pyruvate rCBF. Comparison of pyruvate rCBF from coarse (15×15 mm^2) and high resolution (7.5×7.5 mm^2) [1-^{13}C]pyruvate datasets from the same subject. Pyruvate rCBF from coarse resolution images was an average of 5% higher than pyruvate rCBF from high resolution images, with the highest differences located near the arteries, veins, and gray matter.

Figure S3. Regional [1-^{13}C]pyruvate and total carbon rCBF correlations. Pyruvate rCBF versus total carbon rCBF correlation coefficients and scatterplots for voxels from all subjects ($n = 4$) acquired at high resolution ($n = 5$), by respective mask (3006 whole brain, 1162 gray matter, and 575 white matter voxels all from 2 central slices of the brain). Total carbon rCBF was calculated using summed pyruvate, lactate, and bicarbonate images. Linear regression fits are plotted in red. Total carbon rCBF and pyruvate rCBF correlation was nearly equal to 1. All units are arbitrary.

Figure S4. Regional ASL and [1-^{13}C]pyruvate rCBF correlations for coarse and high pyruvate resolution data acquired in the same subject. Pyruvate rCBF versus ASL rCBF linear correlation coefficients and scatterplots for voxels from one subject acquired at coarse and high resolutions, by respective mask (666 whole brain, 145 gray matter, and 142 white matter voxels all from 2 central slices of the brain). The $15 \times 15 \times 15$ mm^2 coarse resolution pyruvate rCBF correlations with ASL rCBF are all lower than the $7.5 \times 7.5 \times 15$ mm^2 high resolution pyruvate rCBF correlations. For the whole brain correlations, several coarse resolution voxels exhibited high pyruvate rCBF > 0.1 a.u. while only one high resolution voxel exhibited pyruvate rCBF > 0.1 a.u., indicating a reduction in partial volume effects from cerebral blood vessels for high resolution pyruvate data. Voxels with pyruvate rCBF > 0.25 a.u. were excluded due to their being within the superior sagittal sinus and cerebral arteries. Asteriks indicate significant correlation coefficients ($p < 0.05$).

Table S1. Study wise averages and standard deviations ($n = 5$) of Pearson correlation coefficients for whole brain voxels. Averages were calculated using Fisher transformation.

Table S2. Study wise averages and standard deviations ($n = 5$) of Pearson correlation coefficients for gray matter voxels. Averages were calculated using Fisher transformation.

Table S3. Study wise averages and standard deviations ($n = 5$) of Pearson correlation coefficients for white matter voxels. Averages were calculated using Fisher transformation.